Synergistic effect of glucagon-like peptide-1 analogue liraglutide and ZnO on the antibacterial, hemostatic, and wound healing properties of nanofibrous dressings

Fan Wu,[1,‡] Zhengchao Yuan,[1] Muhammad Shafiq,[1,2,‡] Lixiang Zhang,[3] Muhammad Rafique,[4] Fan Yu,[1] Mohamed EL-Newehy,[5] Hany EL-Hamshary,[5] Yosry Morsi,[6] Yuan Xu,[3] and Xiumei Mo[1,*]

State Key Laboratory for Modification of Chemical Fibers and Polymer Materials, Shanghai Engineering Research Center of Nano-Biomaterials and Regenerative Medicine, College of Chemistry, Chemical Engineering and Biotechnology, Donghua University, Shanghai 201620, PR China,[1] Department of Chemical Engineering, Faculty of Engineering, Graduate School, Kyushu University, 744 Motooka, Nishi-ku, Fukuoka 819-0395, Japan,[2] Xinqiao Hospital, Army Military Medical University, No. 183, Xinqiao Street, Shapingba District, Chongqing 400037, China,[3] Key Laboratory of Bioactive Materials, Ministry of Education, College of Life Sciences, Nankai University, Tianjin 300071, China,[4] Department of Chemistry, College of Science, King Saud University, P.O. Box 2455, Riyadh 11451, Saudi Arabia,[5] and Faculty of Engineering and Industrial Sciences, Swinburne University of Technology, Boroondara, VIC 3122, Australia[6]

Bacterial infections and poor vascularization delay wound healing, thus necessitating alternative strategies for functional wound dressings. Zinc oxide (ZnO) has been shown to exert a potent antibacterial effect against bacterial species. Similarly, Glucagon-like peptide-1 (GLP-1) analogue liraglutide (LG) has been shown to promote vascularization and improve wound healing. The objective of this research was to investigate the synergistic effect of ZnO nanoparticles (ZnO-NPs) and LG to simultaneously induce antibacterial, hemostatic, and vascularization effects for infected wound healing. Electrospun poly (L-lactide-co-glycolide)/gelatin (PLGA/Gel) membranes containing ZnO-NPs and LG displayed good biocompatibility and hemostatic ability. Both, ZnO-NPs and LG exhibited synergistic antibacterial effect against *Staphylococcus aureus* and *Escherichia coli* as well as improved the migration and tubule-like network formation of human umbilical vein endothelial cells (HUVECs) *in vitro*. Once evaluated in a bacterial-infected wound model in rats, the membranes loaded with ZnO-NPs and LG effectively promoted wound healing causing significant reduction in wound area and scar-like tissue formation. Therefore, ZnO-NPs/LG synergism may offer an invaluable solution for the treatment of poorly healing infected wounds.

© 2022, The Society for Biotechnology, Japan. All rights reserved.

[**Key words:** Wound healing; Antibacterial; Zinc oxide; Liraglutide; Nanofiber; Biomaterials; Tissue engineering; Skin; Dressings; Glucagon-like peptide-1 (GLP-1)]

The skin is one of the largest organs in the human body which constitutes about 16% of the body weight. Skin tissues are often damaged for up to varying degrees by a myriad of factors, including an external environment, burn, trauma, or a chemical hazard. Being vascularized and innervated, skin tissues exhibit inherent reparative capabilities (1). Inspite of this, chronic wounds are difficult to be healed, which often require an appropriate treatment for scarless wound healing. The main reason for the transition of an acute wound into a chronic non-healing wound is infection, which tends to occur in every type of wound. Though a series of strategies has been put forwarded, including the use of multifunctional hydrogels and nanofibers as dressings for infected wounds, there is still an unmet clinical challenge to design a wound dressing with an optimum bioactivity (2).

Electrospun membranes are widely used as dressings, thanks to their good porosity and high specific surface area, which not only facilitate mass transfer but also endow a moist environment to the wound surface (3). Poly(L-lactide-co-glycolide) (PLGA) has garnered considerable attention of the research community for tissue engineering owning to its tunable degradability and good mechanical strength. However, being devoid of cell recognition cues, PLGA-based scaffolds require modification with bioactive cues, such as extracellular matrix proteins or peptides to encourage cellular infiltration as well as induce tissue remodeling (3–5). Gelatin (Gel) exhibits good biocompatibility, cell recognizability, and biodegradability and has been exploited to afford PLGA/Gel membranes for wound healing (6–8).

Glucagon-like peptide-1 (GLP-1R) is a 30-amino acid residue, which mediates its antihypertensive, hypoglycemic, anti-inflammatory, antioxidative and angiogenesis-promoting effects by interacting with GLP-1 receptor (GLP-1R); the latter is expressed in various types of tissues, including intestine, lung, and innate immune system. However, the rapid degradation of GLP-1 by dipeptidyl peptidase IV (DPP-IV) (half-life, 2 min) limits its clinical applications. GLP-1 analogues resistant to the degradation by DPP-IV have been shown to interact with GLP-1R. Liraglutide (LG), a palmityl-acetylated derivative of GLP-1 is being used as a therapeutic for the treatment of type 2 diabetes mellitus and has been shown to exhibit anti-inflammatory and anti-oxidative properties (9,10). Moreover, LG promotes the migration of multiple types of cells, including keratinocytes and human umbilical vein endothelial

cells (HUVECs) as well as improves wound healing by regulating the expression of angiogenic growth factors (9–11). However, the poor water solubility and frequent administration limit the application of LG in tissue engineering.

Besides, inorganic nanomaterials such as zinc oxide (ZnO) have been exploited for antibacterial applications (12). ZnO nanoparticles (ZnO-NPs) exhibit an adequate antibacterial activity without ultraviolet (UV) irradiation (13). ZnO-NPs releases free zinc ions (Zn^{2+}), which can electrostatically accumulate on the surface of bacterial membranes, thereby inducing an antibacterial effect (14). Moreover, ZnO-NPs can induce the production of reactive oxygen species to exacerbate oxidative stress, which may further lead to the killing of the bacterial cells. While wound dressings containing ZnO-NPs have been shown to exhibit good antibacterial potential, they still require additional therapeutic modalities to promote scar-less skin regeneration. A combinatorial use of angiogenesis-promoting factors along with ZnO-NPs could obviate these limitations. Owning to its obvious angiogenesis promoting effects as well as its ability to regulate cellular processes, LG offers an enticing platform to induce vascularization for wound healing.

Hitherto, we assessed the synergistic effect of LG and ZnO-NPs for skin regeneration. PLGA/Gel membranes encapsulating LG and ZnO-NPs (PGZL) were fabricated by electrospinning and their potential was examined *in vitro* as well as *in vivo* in an infection wound model in rats. Once LG and ZnO-NPs were co-loaded into PLGA/Gel membranes, they showed good biodegradability, biocompatibility, and hemocompatibility, which not only remarkably improved cellular processes, such as cell proliferation and migration, but also promoted the formation of tubule-like networks of HUVECs *in vitro*. The biocompatibility of the nanofibrous membranes also revealed a good potential for wound healing in terms of wound closure, scar length reduction, and fast wound healing rate. Therefore, these nanofibrous membrane may have broad implications for wound healing applications and are worthy of future investigations.

MATERIALS AND METHODS

Preparation of nanofiber membranes   Firstly, PLGA (LA:GA = 50:50, M_w = 95 kDa, Jinan Daigang Biomaterial Co., Ltd., Jinan, China) and Gelatin (Gel, type B, MP Biomedicals, LLC, Shanghai, China) were dissolved in 1,1,1,3,3,3-hexafluoro-2-propanol (HFIP, 99.5%, Shanghai Darui Fine Chemical Co., Ltd., Shanghai, China) to afford 20 wt% PLGA/Gel (PG, PLGA:Gel, 7:3 w/w) solution, and stirred for 12 h to afford a stable spinning solution. Thereafter, ZnO-NPs (size ≤40 nm, Sigma−Aldrich, St. Louis, MO, USA) (1 wt% with respect to the total polymer weight) were added into the PG solution to afford PGZ. Lastly, different concentrations of LG (purity, 99%, Baishikai Chemicals, Shanghai, China) were added into PGZ solution (0.05, 0.10, and 0.15 wt% with respect to the polymer weight) and further stirred for up to 12 h to afford a homogenous dispersion, which were named as PGZL-1, PGZL-2 and PGZL-3, respectively.

The PG, PGZ, PGZL-1, PGZL-2, and PGZL-3 membranes were fabricated by electrospinning (SS-3556H, Yongkang Leye Technology Development Co., Ltd., Beijing, China) with the parameters as follows: needle size, 21G, syringe pump size, 10 mL, voltage, 10 kV, flow rate, 1.5 mL/h, collector speed, 2000 rotations per minute (rpm), and distance between spinneret jet and collector, 10-cm, temperature, ∼25 °C, relative humidity, 45−50%, and collector, an aluminum foil. The prepared membranes were stored at 4 °C.

Characterization of nanofiber membranes   Scanning electron microscopy (SEM, Hitachi, TM-1000, Japan) along with an Energy dispersive X-ray spectroscopy (EDX) was used to analyze the morphology and elemental distribution of membranes. The average fiber diameter and pore size of membranes were computed by using ImageJ software (National Institute of Health) and a CFP-1100-AI capillary flow porometer (PMI Porous Materials Inc., Ithaca, NY, USA), respectively. Water contact angle (WCA) was measured by a WCA meter (DSA 100, Krüss, Hamburg, Germany) and analyzed by ImageJ software. Thermal stability was evaluated in an inert atmosphere by using thermogravimetric analyzer (SQ8-STA8000, PerkinElmer, Waltham, MA, USA) from 50 to 800 °C at a flow rate 10 °C/min.

The porosity (P) of membranes (20 mm × 20 mm × 0.2 mm) was assessed by the liquid displacement method using absolute ethanol following Eq. 1 (4):

$$P = \frac{(W_t - W_0)}{\rho \times V} \tag{1}$$

where ρ and V represent the density and volume, respectively. The W_0 and W_t represent the weight of membranes at $t = 0$ and 6 h, respectively.

The structural analysis of membranes was performed by using Fourier transform infrared spectroscopy (FTIR) in the range of 2200−600 cm^{-1}. The remaining mass of membranes after incubation in PBS for up to 5 weeks was calculated by Eq. 2:

$$\text{Remaind mass } (\%) = \frac{m_t}{m_0} \times 100 \tag{2}$$

where m_0 and m_t represent the mass of membranes at the beginning and at the predetermined time points, respectively.

Mechanical testing   Mechanical properties of rectangular-shaped membranes (10 mm × 30 mm) were assessed by universal material testing machine (HY-940FS, Hyclone, Logan, UT, USA) containing a load cell of 200 N (BAB-20MT, Transcell Technology, Inc., Buffalo Grove, IL, USA). Ultimate tensile strength (UTS), Young's modulus (E), and elongation at break (Eb) were computed from stress-strain curves ($n = 5$).

Cytotoxicity and cytocompatibility   The cytotoxicity of LG against HUVECs (Typical Culture Collection Committee Cell Bank, Chinese Academy of Science, Shanghai, China) was evaluated by using cell counting kit 8 (CCK-8) assay (Solarbio Science & Technology Co., Ltd., Beijing, China). Varying doses of LG (1 ng/mL to 100 μg/mL) were co-cultured along with HUVECs (1.0×10^4 cells/well) at 37 °C in an incubator with 5% CO_2 ($n = 3$). At 24 h and 48 h, the absorbance was measured at 450 nm (Thermo Fisher Multiskan FC, Thermo Fisher Scientific, Waltham, MA, USA). For cytocompatibility, HUVECs (1.5×10^4 cells/well) were seeded on sterilized scaffolds ($n = 3$, γ-rays irradiated by Co-60, 6 h) for up to 1, 3, and 7 days, and the complete medium (89% Dulbecco's modified Eagle's medium high-glucose supplemented with 1% of 100 U/mL penicillin, 0.1 mg/mL of streptomycin and 10% fetal bovine serum, Gibco Life Technologies, Co., Waltham, MA, USA) was changed every other day. Cell-seeded constructs were incubated at 37 °C, 5% CO_2 ($n = 3$). Cell proliferation and cell viability of membranes were examined by CCK-8 assay and live/dead assay, respectively ($n = 3$). Scaffolds were stained with a live/dead cell imaging kit at day 1, 4 and 7 and observed by microscope (TS100, Nikon, Tokyo, Japan).

Scratch wound healing assay *in vitro*   Cell migration *in vitro* was evaluated by scratch wound healing assay (4). HUVECs (1.5×10^4 cells/well) were seeded on a 24-well plate ($n = 3$). Wound scratches were created by the tip of 1 mL pipette followed by the removal of debris and the addition of low-serum medium containing 1% FBS. Cell migration at 0 h and 24 h was observed under a light microscope and the wound closure was quantified by ImageJ by Eq. 3:

$$\text{Wound closure (\%)} = \frac{A_t}{A_0} \times 100 \tag{3}$$

where A_0 and A_t indicate the initial scratch area and healed scratch area at a predetermined time point, respectively.

Tube formation assay *in vitro*   The BD Matrigel (356,234, BD Biosciences, Franklin Lakes, NJ, USA) was prepared at 4 °C overnight (4). About 50 μL of Matrigel was added to the bottom of a pre-cooled 96-well plate, and then incubated at 37 °C, 5% CO_2 for 30 min. The conditioned medium (obtained by incubating membranes in FBS-containing DMEM at 37 °C for up to 24 h) and HUVECs (1.0×10^4/well) were added onto Matrigel and incubated for 6 h ($n = 3$). The tube formation was observed by a light microscope. The ImageJ was used to quantify the number of nodes, circles, and total branching length. The total branch length of PG group was chosen as a reference and was compared with the other groups to afford the normalized total branching length.

Antioxidative activity   Antioxidative activity of membranes was evaluated by 2,2-diphenyl-1-picrylhydrazyl (DPPH) assay ($n = 3$). Membranes (weight, ∼10 mg) were placed in 3 mL of DPPH solution (0.1 mmol/L in ethanol) for up to 30 min. Absorbance (B_{sample}) of each group of solution as well as DPPH solution (B_0) was recorded at 517 nm. The free radical scavenging rate (RSR) was calculated by Eq. 4:

$$\text{RSR \%} = \frac{B_0 - B_{sample}}{B_0} \times 100 \tag{4}$$

where B_0 and B_{sample} represent the absorbance of DPPH solution and sample solution, respectively.

Antibacterial activity   Antibacterial properties of membranes were evaluated by using gram-positive bacteria, *Staphylococcus aureus* (ATCC 25923) and gram-negative bacteria *Escherichia coli* (ATCC 2592) (Chinese Academy of Sciences, Shanghai, China). Membranes ($n = 3$, 15 mm × 15 mm) were sterilized by UV irradiation for up to 12 h. Both types of bacteria were transferred to bacterial cell culture medium (LB Broth, LB Broth Agar, Sangon Biotech, Shanghai, China) for up to 12 h and incubated at 37 °C to afford a bacterial concentration of 10^5 CFU/mL. Thereafter, about 1 mL of the bacterial culture solution was evenly spread on membranes and incubated at 37 °C for 24 h. All of the bacterial culture solution
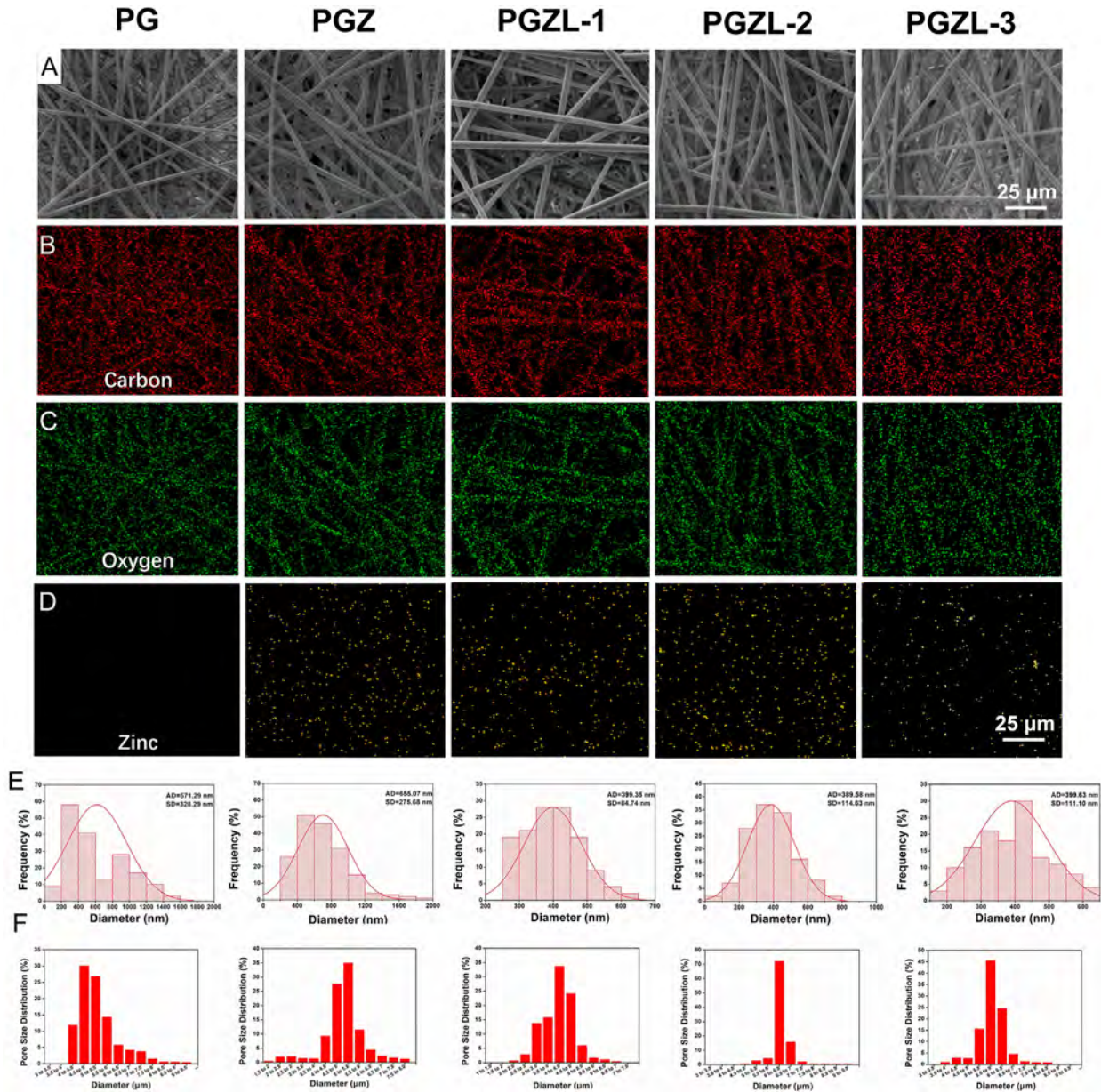
FIG. 1. Morphological analysis of membranes. (A) SEM micrographs and (B–D) elemental distribution. (E) Diameter distribution and (F) pore size distribution. Scale bar: 25 μm (A–D).

was transferred to 10 mL of PBS. After dilution, 10^3 CFU/mL bacterial culture solution was obtained, which was evenly spread on an agar plate, and the images were taken after incubating the agar plate in an incubator at 37 °C for 24 h. Pure bacterial suspension without membranes was used as a blank control group.

Hemocompatibility and blood coagulation assay   Membranes (10 mm × 10 mm) were pre-heated at 37 °C for up to 5 min in a Petri dish ($n = 3$). Rabbit whole blood (0.25 mL) was added onto membranes and incubated at 37 °C for 1 min. Once rinsed with 3 mL of deionized water and incubated at 37 °C for 10 min, the solution was collected and centrifuged at 800 rpm for 5 min. The absorbance of the supernatant (OD_t) and the fresh blood (OD_0) was measured at 545 nm. The blood clotting index (BCI) was calculated by Eq. 5 ($n = 3$):

$$\mathrm{BCI}\ (\%) = \frac{OD_t}{OD_0} \times 100 \tag{5}$$

The fresh rabbit whole blood was centrifuged at 3000 rpm for 15 min to obtain platelet poor plasma (PPP). Membranes (10 mm × 10 mm) were incubated with 100 μL of PPP at 37 °C for 2 min ($n = 3$). For pro-thrombin time (PT), PT reagent (100 μL) was added to the incubated samples, and the time taken for PPP to the clotting was recorded. For activated partial thromboplastin time (APTT) assay, membranes were incubated with 100 μL of APTT at 37 °C for 3 min, then 0.025 M CaCl$_2$ solution was

added (100 μL) and the blood clotting time was recorded. Thereafter, APTT, PT, and clotting time were measured ($n = 3$).

Hemocompatibility of membranes   For hemolysis, about 5 mL of fresh rabbit whole blood was centrifuged at 3000 rpm for 15 min to obtain the lower layer of red blood cells (RBCs). The erythrocytes were suspended in PBS (erythrocytes vs. PBS, 4:5, v/v) and 1 mL of the RBCs suspension was incubated with membranes (10 mm ×10 mm) at 37 °C for 2 h. Thereafter, the cell suspension was centrifuged at 3000 rpm for 10 min, and the supernatant was collected to measure the optical density (OD) at 540 nm. PBS and deionized water were used as negative and positive controls, respectively and the hemolysis ratio was ascertained by Eq. 6 ($n = 3$):

$$\mathrm{Hemolysis\ ratio}\ (\%) = \frac{A_S - A_N}{A_P - A_N} \times 100 \tag{6}$$

The A_S represents the OD value of the sample, while A_P and A_N indicate the OD values of the positive and negative controls, respectively.

Wound healing in vivo   The reparative ability of membranes was further assessed in a rat skin defect model infected with S. aureus by following the guidelines of the Institutional Animal Care and Use Committee (IACUC) of the Army Military Medical University. Animals were anesthetized by injecting 10% of chloral
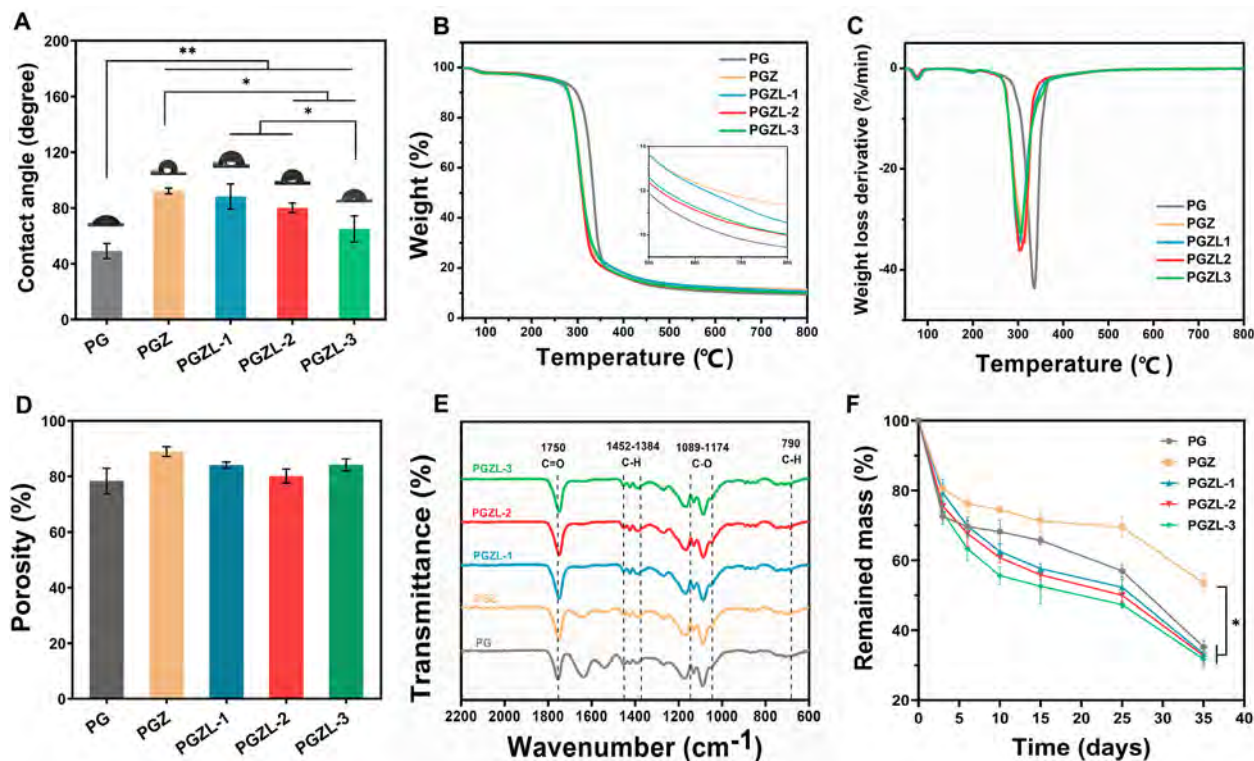
FIG. 2. Physico-chemical analysis of membranes. (A) WCA, (B) TGA and (C) DTG curves, (D) porosity, (E) FTIR spectra, and (F) degradation. $*p < 0.05$ and $**p < 0.01$.

hydrate (300 mg·kg^{-1}). Thereafter, the skin was shaved, and defects (diameter, 10 mm) were created. Bacterial infection model was prepared by injecting 200 μL of *S. aureus* suspension (10×10^8 CFU/mL) into each wound. Sterilized membranes ($n = 3$, 10 mm × 10 mm) were affixed on the wound surface. The wounds which were left untreated served as controls. At day 0, 3, 7, and 10, the wounds were observed and photographed. The wound area was tracked by ImageJ, and the wound closure rate was calculated by Eq. 7:

$$\text{Wound area (\%)} = \frac{A_t}{A_0} \times 100 \qquad (7)$$

The A_0 and A_t depict the wound area at day 0 and at day 3, 7, and 10, respectively.

Statistical analysis Data were expressed as mean ± standard deviation. All data were analyzed by one-way ANOVA with Tukey's *post hoc* tests. Statistical significance was considered at $p < 0.05$ and $p < 0.01$.

RESULTS

Preparation and characterization of nanofibers As shown in Fig. 1, ZnO-NPs and LG were encapsulated into PLGA/Gel nanofibrous membranes by electrospinning. SEM micrographs revealed the uniform morphology of nanofibers exhibiting a smooth surface as well as a porous structure (15). EDS photographs further revealed the uniform dispersion of C, O and Zn in PGZ, PGZL-1, PGZL-2, and PGZL-3 nanofibers; the PG membranes lacked zinc content (Fig. 1A–D). The average fiber diameter of the PG, PGZ, PGZL-1, PGZL-2, and PGZL-3 nanofibrous membranes was found to be 571.3 ± 328.3 nm, 655.1 ± 276.0 nm, 399.4 ± 84.7 nm, 390.0 ± 114.6 nm, and 400.0 ± 111.1 nm, respectively (Fig. 1E). The LG containing membranes showed a slight reduction in the fiber diameter than that of the PG and PGZ membranes. Since the α-helices of LG are amphiphilic, containing a hydrophobic and a hydrophilic terminal, its interaction with both hydrophobic PLGA and hydrophilic gelatin may have induced a minute reduction in the fiber diameter. On the other hand, while ZnO-NPs had a little effect on the pore size of nanofiber, the incorporation of LG

increased the pore size of membranes (Fig. 1F), which may be beneficial for cellular infiltration into scaffold materials (8).

The WCA can be used to characterize the hydrophilicity or hydrophobicity of the scaffolds. The WCA of membranes is shown in Fig. 2A. PG exhibited good hydrophilicity as evidenced by its low WCA value (49.10 ± 5.41°). On the other hand, the hydrophilicity of PG was decreased with the addition of ZnO-NPs; the WCA of PGZ was found to be 92.14 ± 2.06°. This may be ascribed to the delayed absorption of water droplets by the ZnO-NPs loaded membranes. While the WCA of PGZ decreased with the addition of LG (WCA values: PGZL-1, 88.17 ± 0.03° and PGZL-2, 80.12 ± 3.46°), it was still higher than that of the PG. The WCA of PGZL-3 was about 66.32 ± 8.72°, indicative of the good hydrophilicity of these membranes. These data show that the LG can decrease the WCA of membranes. The good hydrophilicity of LG-loaded membranes may be beneficial for cell adhesion and migration.

Fig. 2B and C shows TG and DTG thermograms of electrospun membranes. As can be seen from these data, the membranes displayed a single-step mass loss mainly in the range of 150−450 °C. Membranes containing ZnO-NPs and LG exhibited less thermal stability than that of PG. For instance, the temperature corresponding the 10% mass loss was found to be 297.4 °C, 279.0 °C, 280.3 °C, 281.3 °C, and 279.8 °C for PG, PGZ, PGZL-1, PGZL-2, and PGZL-3 membranes, respectively. Similarly, the temperature corresponding to 50% mass loss was found to be 335.8 °C, 314.3 °C, 309.0 °C, 312.7 °C, and 310.8 °C for PG, PGZ, PGZL-1, PGZL-2, and PGZL-3 membranes, respectively. On the other hand, the residue content of ZnO-NPs containing membranes was slightly higher than that of PG in the range of 500−800 °C, which is attributable to the ZnO-NPs (16,17).

The porosity of the PG group was 78.4 ± 4.5%, while that of PGZ, PGZL-1, PGZL-2, and PGZL-3 membranes was 85.6 ± 2.5%, 84.1 ± 1.1%, 80.2 ± 2.5%, and 84.2 ± 2.1%, respectively. While all of the membranes exhibited porosity values higher than that of 80%, various groups did not significantly differ from each other in terms

of the porosity. It can be seen that the incorporation of ZnO-NPs and LG did not have a significant effect on the porosity of the nanofiber membrane, and that these membranes may be conducive to cellular infiltration and wound healing.

The composition and chemical structure of membranes were analyzed by FTIR (Fig. 2E). It can be seen from the FTIR spectra that the membranes exhibited bands in the range of 1789–1730 cm^{-1}, 1452–1384 cm^{-1}, and 1174–1089 cm^{-1}, which are ascribed to the carbonyl (C=O) stretching vibration, C–H bending vibration, and C–O stretching vibrations of PLGA, respectively. The addition of LG did not generate new bands, which indicate that it has been physically mixed into nanofiber membranes.

The degradation of membranes was evaluated by using PBS at 37 °C for up to 5 weeks in vitro (Fig. 2F). All groups experienced significant weight loss over time. After 5 weeks of incubation in PBS in vitro, PGZ membranes almost lost 50% of their initial weight (remained mass, PGZ, 53.48 ± 2.40%). On the other hand, PG, PGZL-1, PGZL-2, and PGZL-3 membranes approximately lost 70% of their initial weight by this time point. The remained mass was 35.15 ± 1.54%, 33.24 ± 1.31%, 32.75 ± 1.92%, and 31.71 ± 1.84% for PG, PGZL-1, PGZL-2, and PGZL-3, membranes, respectively. From day 0–14, ZnO-NPs and LG containing membranes displayed faster degradation than that of the PG or PGZ membranes (remained mass, PG, 65.67 ± 0.99%, PGZ, 71.24 ± 2.73%, PGZL-1, 57.63 ± 1.20%, PGZL-2, 55.83 ± 1.20%, and PGZL-3, 52.57 ± 4.084%), which may be ascribed to the incorporation of LG. We have noticed a concomitant reduction in the WCA of PGZ membranes with an increase in the LG content, which may be attributable to LG-mediated increase in the

hydrophilicity. The earlier degradation of membranes may be beneficial to not only facilitate cellular infiltration but also to lessen the secondary damage to the wound surface.

Mechanical testing   Fig. 3A shows representative stress-strain curves of the membranes. With the addition of ZnO-NPs, the E and Eb of membranes were decreased (Fig. 3B and D), while UTS was increased (Fig. 3C). However, with the addition of LG, E, UTS and Eb of membranes were slightly increased. The reduction in the tensile properties of membranes with the incorporation of ZnO-NPs may be attributed to the poor compatibility between polymer matrix and nanoparticles. While ZnO-NPs containing membranes displayed lower tensile properties than that of the PG group, these membranes exhibited enough mechanical properties for wound repair according to previous research (8,13,14).

Biocompatibility of membranes in vitro   To further elucidate a dose-dependent effect of LG on cell proliferation, varying concentrations of drug in the range of 0.001–100 μg/mL were co-cultured along with HUVECs in vitro. HUVECs exhibited good proliferation at all studied concentrations, indicative of the good cytocompatibility of LG (Fig. 4A). We next ascertained the biocompatibility of ZnO-NPs and LG containing membranes by using HUVECs. Cell proliferation was assessed by CCK-8 assay at day 1, 4, and 7 after incubation (Fig. 4B). By the day 1, ZnO-NPs and LG containing membranes (e.g., PGZL-1, PGZL-2 and PGZL-3) displayed less OD values than that of the PG and PGZ membranes. With the passage of time, the cell proliferation was significantly increased in each group. While there was an
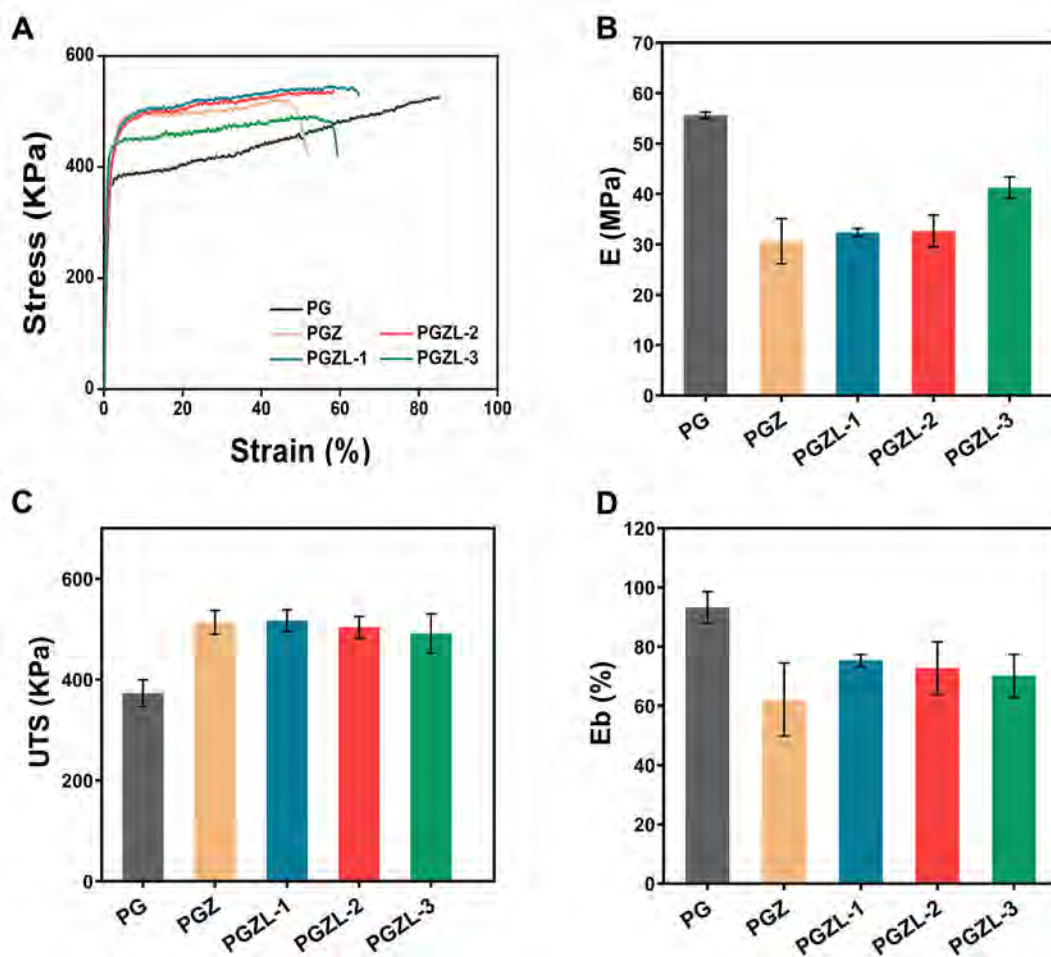

FIG. 3. Mechanical properties of membranes. (A) Stress-strain curves, (B) Young's modulus, (C) UTS, and (D) Eb ($n = 5$).
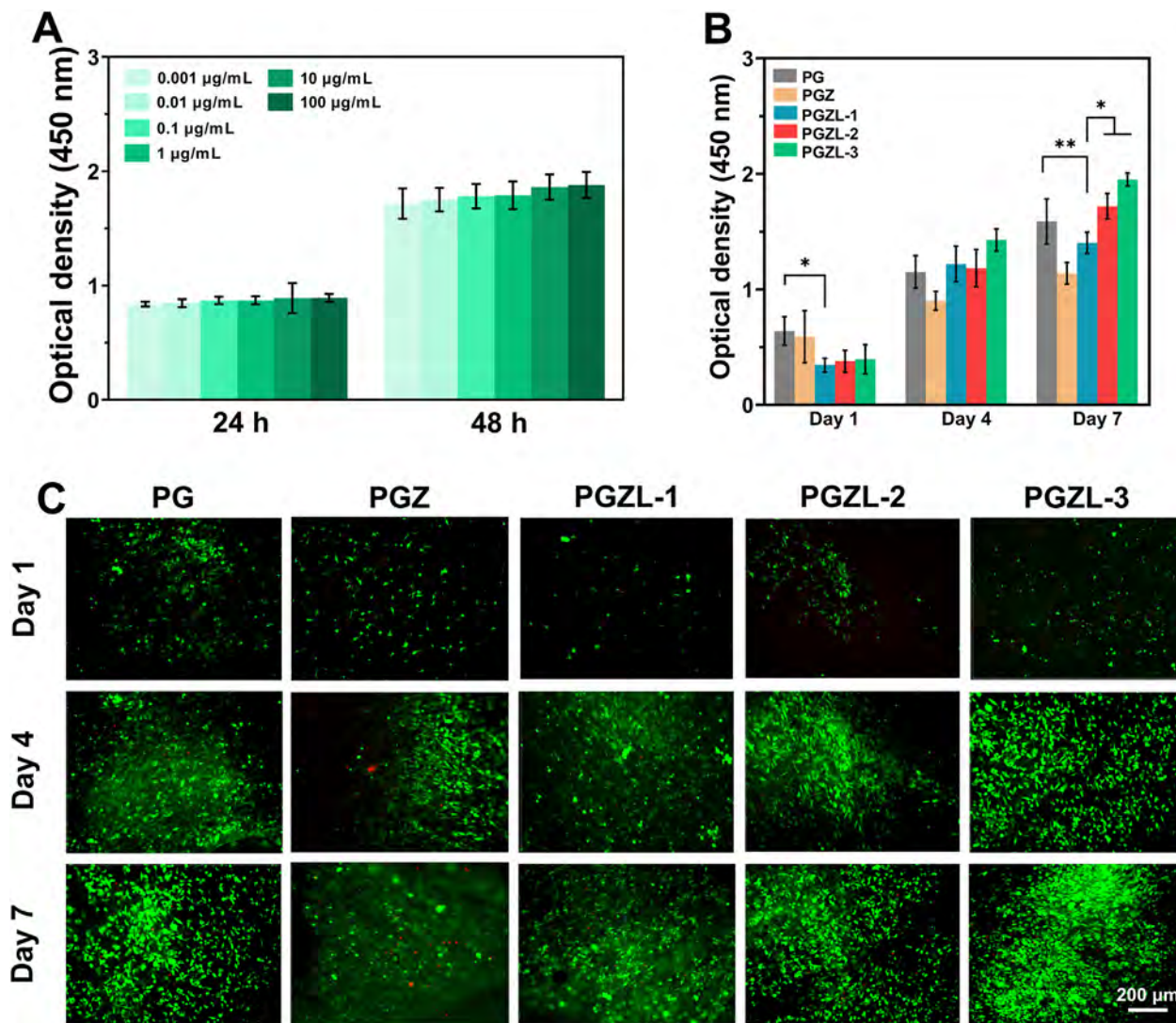
FIG. 4. Biocompatibility of membranes *in vitro*. Proliferation of HUVEC cultured with varying doses of LG (A) and with membranes (B). (C) Live/dead assay. Scale bar: 200 μm ($n = 3$). *$p < 0.05$ and **$p < 0.01$.

insignificant difference among the groups by day 4 in terms of the cell proliferation, PGZL-2 and PGZL-3 membranes displayed significantly higher cell proliferation rate than that of the other groups by the day 7. Live/dead assay further delineated good viability of cells (Fig. 4C). There were more numbers of live cells (stained in the green colour) on the membranes in each group, while there were only a few numbers of dead cells (stained in the red colour). Besides, HUVECs displayed a typical spindle-shaped morphology, and the live cell density on ZnO-NPs and LG containing membranes was the highest than that of the PG and PGZ membrane at day 4 and 7. This reflects the good biocompatibility of membranes.

Scratch wound healing assay and tube formation assay A scratch wound healing assay was performed to discern the effect of the membranes on the migration of HUVECs *in vitro* (Fig. 5A). While membranes loaded with ZnO-NPs (PGZ group) displayed significantly high extent of wound closure, those containing both ZnO-NPs and LG showed synergistic effect on HUVECs migration *in vitro* as well as displayed significantly higher cell migration than that of the PG and PGZ membranes (Fig. 5C). It has been previously reported that the LG can promote the

migration of various types of cells, such as keratinocytes and HUVECs by modulating GLP-1/GLP-1R axis via PI3K/Akt and AKT/GSK-3β/β-catenin pathways (8).

To evaluate the ability of membranes to promote tube formation in HUVECs, the conditioned medium was obtained from different membranes and incubated along with HUVECs (Fig. 5B). Membranes loaded with ZnO-NPs and LG exhibited significantly higher numbers of nodes (Fig. 5D), circles (Fig. 5E) and total branching length (Fig. 5F) than that of the PG and PGZ membranes, thereby illustrating a synergistic effect between ZnO-NPs and LG to promote angiogenesis *in vitro*. It has been reported that the LG can promote the VEGF secretion of HUVECs as well as induce the phosphorylation of Akt, thereby facilitating angiogenesis *in vitro* and *in vivo* (8).

Blood coagulation and hemocompatibility *in vitro* APTT and PT were measured to delineate the blood coagulation and hemocompatibility of membranes *in vitro*. As can be seen from Fig. 6A, membranes containing ZnO-NPs (PGZ group) exhibited significantly less APTT values than that of the PG membranes, which became further pronounced in membranes containing both ZnO-NPs and LG. Similarly, the PT values of the membranes
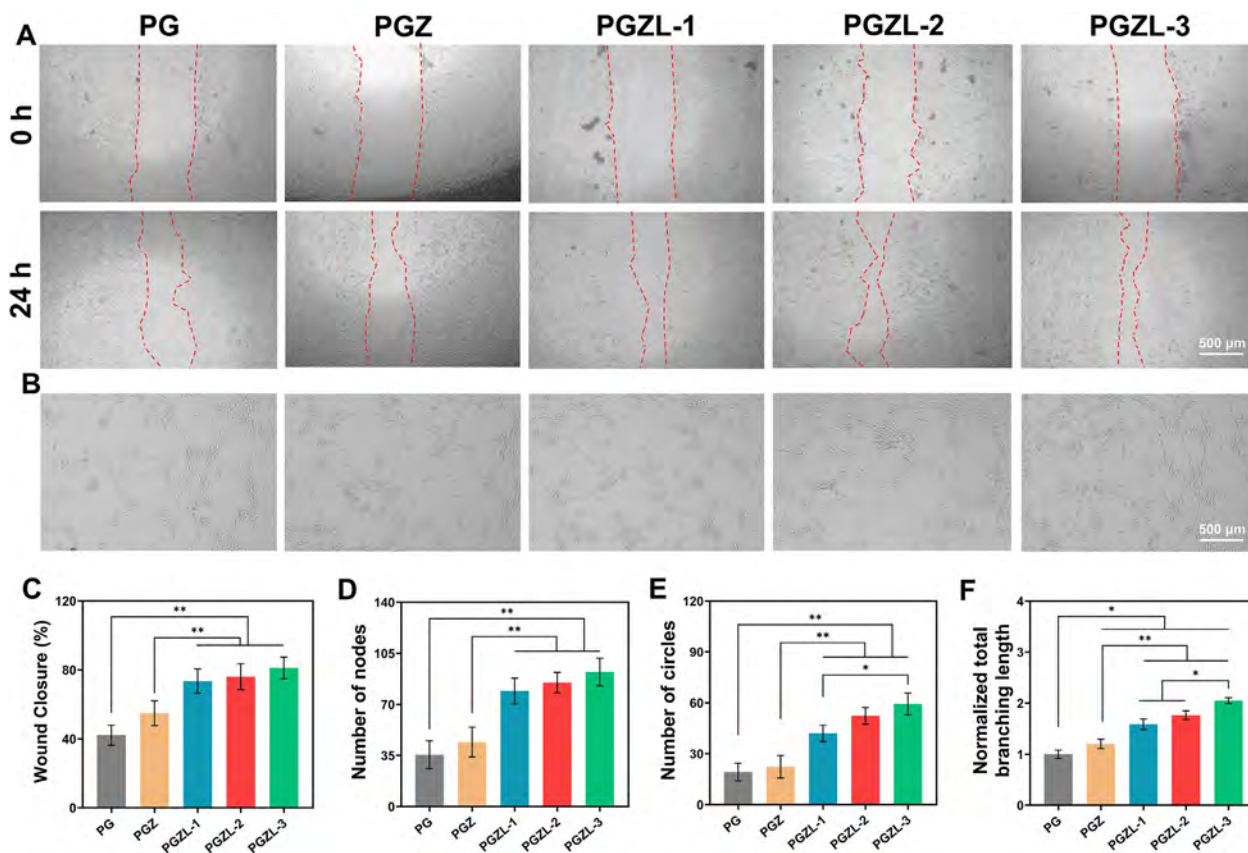
FIG. 5. *In vitro* cell migration assay and tube formation assay. (A) Cell migration, (B) tube formation assay, (C) wound closure, and (D–F) angiogenic parameters. Scale bar: 500 μm (A, B) ($n = 3$). *$p < 0.05$ and **$p < 0.01$.

containing ZnO-NPs were lower than that of the PG membranes, and the PGZL-3 membranes exhibited significantly lower PT value than that of the other groups (Fig. 6B). This reduction in the APTT and PT values of membranes can be attributed to ZnO-NPs; zinc can mediate the phosphorylation of the platelet protein tyrosine through protein kinase C (18), enhancing platelet activity and aggregation (19), and thereby accelerating hemostasis. These results indicate that both ZnO-NPs and LG acted synergistically, which may also activate intrinsic and extrinsic coagulation pathways, thereby affecting the coagulation process, which may have implications for wound healing *in vivo*.

To further assess the hemocompatibility of membranes, hemolysis assay was performed. The macroscopic images of the hemolysis assay for negative control group (normal saline), positive control group (deionized water) and membranes are shown in Fig. 6C. Except for the positive control group, the supernatants obtained from all of the other groups were similar to the negative control group, showing a colorless and a transparent state. Fig. 6D shows that the hemolysis rate of each group of the membranes was below 2%, which is in line with the national standard (4,8). These results indicate the good hemocompatibility of membranes.

The hemostatic effect of the membranes on the wound surface was next evaluated by the blood clotting index (BCI). Fig. 6E visually shows the coagulation process of nanofibrous membranes. With the incorporation of ZnO-NPs as well as with an increase in the LG content, the BCI of membranes showed a decreasing trend (Fig. 6F). The BCI values of PGZ, PZGL-1, PGZL-2, and PGZL-3 membranes were significantly lower than that of the PG group, indicative of the good hemostatic ability of ZnO-NPs and LG containing membranes (Fig. 6F). Amongst, PGZL-3 membranes exhibited the highest hemostatic ability.

Antioxidative activity The antioxidative capacity of the nanofibrous membranes was investigated by DPPH assay. The free radical scavenging rate was found to be $17.5 \pm 6.4\%$, $39.9 \pm 6.3\%$, $50.4 \pm 2.1\%$, $59.5 \pm 2.7\%$, and $61.3 \pm 0.5\%$ for PG, PGZ, PGZL-1, PZGL-2, and PGZL-3 membranes, respectively (Fig. 6G). The free radical scavenging rate of nanofiber membranes loaded with ZnO-NPs was significantly higher than that of PG membrane. Similarly, the membranes containing both ZnO-NPs and LG showed significantly higher free radical scavenging rate than that of the PGZ group, which indicated a synergistic effect between ZnO-NPs and LG to promote anti-oxidative properties. These data indicate that the antioxidative ability of the membranes was remarkably improved with the addition of nano-ZnO and LG.

Antibacterial activity Antibacterial properties of membranes were assessed against *E. coli* and *S. aureus* (Fig. 7). Fig. 7A visually shows the growth of bacteria in each group. The survival rate of *E. coli* on PG, PGZ, PGZL-1, PGZL-2 and PGZL-3 membranes was found to be $105.6 \pm 4.9\%$, $20.6 \pm 4.3\%$, $9.3 \pm 4.0\%$, $6.3 \pm 2.5\%$ and $2.0 \pm 0.5\%$, respectively (Fig. 7B). Similarly, the survival rate of *S. aureus* was found to be $106.4 \pm 1.6\%$, $11.7 \pm 2.9\%$, $37.0 \pm 3.7\%$, $17.6 \pm 3.7\%$ and $10.3 \pm 1.4\%$ on PG, PGZ, PGZL-1, PGZL-2 and PGZL-3 membranes, respectively (Fig. 7C). These data show that the membranes loaded with ZnO-NPs and LG had a significant inhibitory effect on both types of bacteria, and the bacterial survival rate was lower than 40%. The inhibitory effect of PGZL-3 on *E. coli* reached for up to 98%, showing a strong antibacterial activity.

Wound healing *in vivo* Having examined the biological properties of membranes, including their anti-oxidative ability, coagulation activity, hemostatic ability, and antibacterial activity
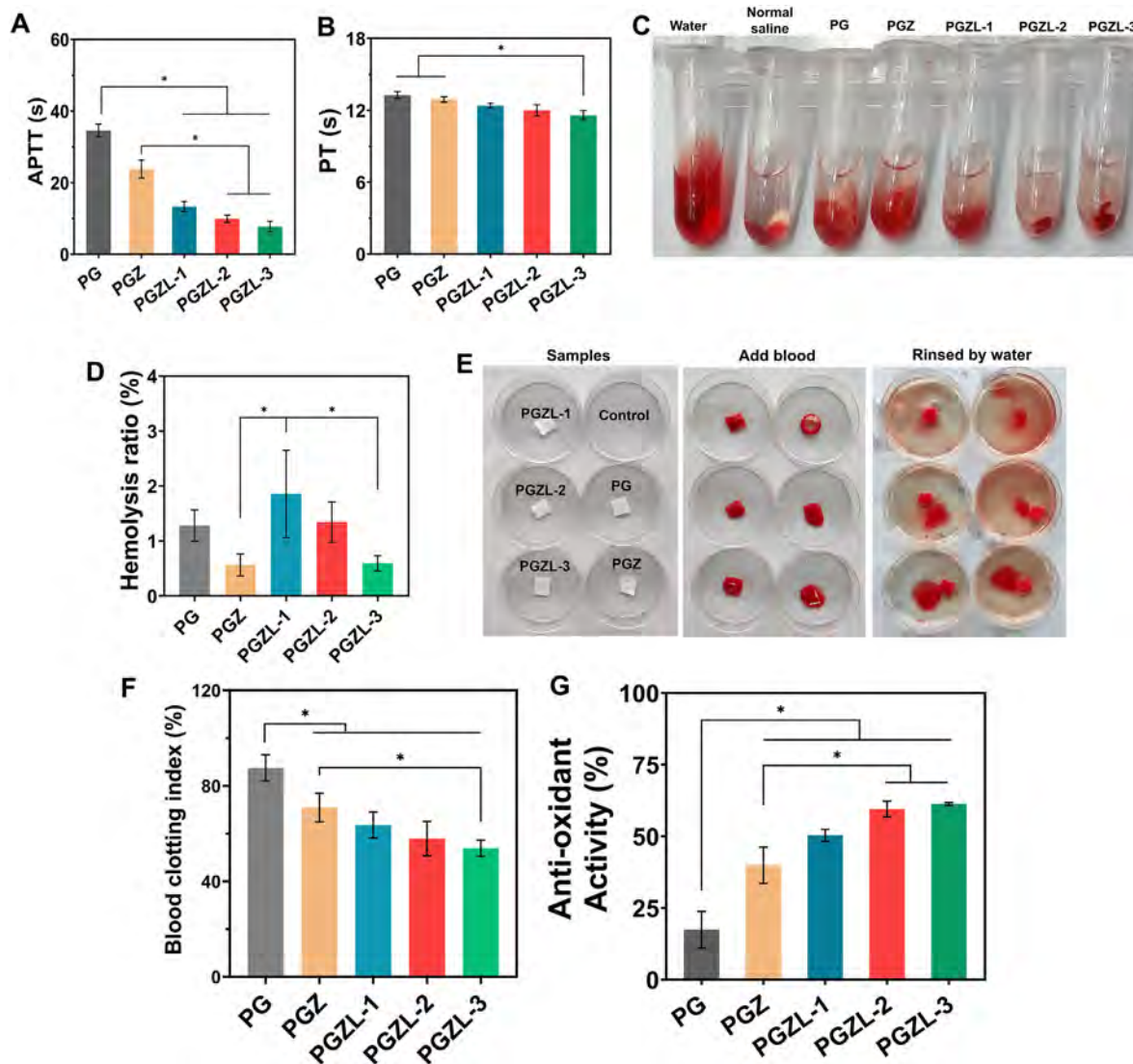
FIG. 6. Hemostatic ability and hemocompatibility of membranes ($n = 3$). (A) APTT, (B) PT, (C) blood compatibility , (D) hemolysis ratio, (E) coagulation process, (F) BCI and (G) antioxidative ability. $*p < 0.05$.

in vitro, we established a bacterial infection model in SD rats to evaluate the ability of membranes to alleviate bacterial infection and promote wound healing (Fig. 8). Fig. 8A shows the wound healing induced by the three types of membranes, including PG, PGZ, and PGZL-3 at day 0, 3, 7, and 10. While after a few days, the wounds in each group were continued to be healed, the wounds treated with ZnO-NPs and LG containing membranes exhibited significantly less wound area, shorter scar length, and higher wound closure rate as compared to the other groups, showing a higher wound healing rate (Fig. 8B–D). While PGZ membranes displayed high wound healing than that of the control and PG groups, those containing both ZnO-NPs and LG displayed significantly higher wound healing than that of the all groups.

DISCUSSION

ZnO-NPs and LG exhibit excellent antibacterial properties and vasculogenic abilities; the latter promotes the phosphorylation of protein kinase AKT (8−10). We have deciphered a synergistic effect between ZnO-NPs and LG to improve wound repair. We leveraged electrospinning to fabricate nanofibrous membranes owing to its

potential to realize extracellular matrix-mimetic scaffolds (20). Morphologically, membranes displayed sufficient porosity and pore size; ZnO-NPs and LG did not have an appreciable effect on the morphology of nanofibers. As shown by the EDS, ZnO-NPs were homogenously dispersed in scaffolds while avoiding the formation of a bead-like or an aggregated structure (Fig. 1). On the other hand, the LG containing fibers displayed broad pore size distribution as well as higher hydrophilicity and biodegradability, which may be beneficial for cell infiltration (8). ZnO-NPs reduced the Eb of PG membranes from 93% to 53%, which reverted to 75% with the incorporation of LG (Fig. 3). It is noteworthy to mention here that the mechanical properties of membranes were in the range of the previous reports as required for wound healing (13,14).

As dressings directly contact the wound microenvironment, they should be biocompatible with the host tissues. Membranes containing ZnO-NPs displayed lower cell proliferation than that of the PG group, which further decreased upon the addition of LG by the day 1. While there was an insignificant difference among different groups in terms of cell proliferation by the day 4, PGZ-2 and PGZ-3 membranes exhibited significantly higher cell proliferation as compared to other groups by the day 7 (Fig. 4B and C). Scratch wound healing assay and tube formation assay *in vitro*
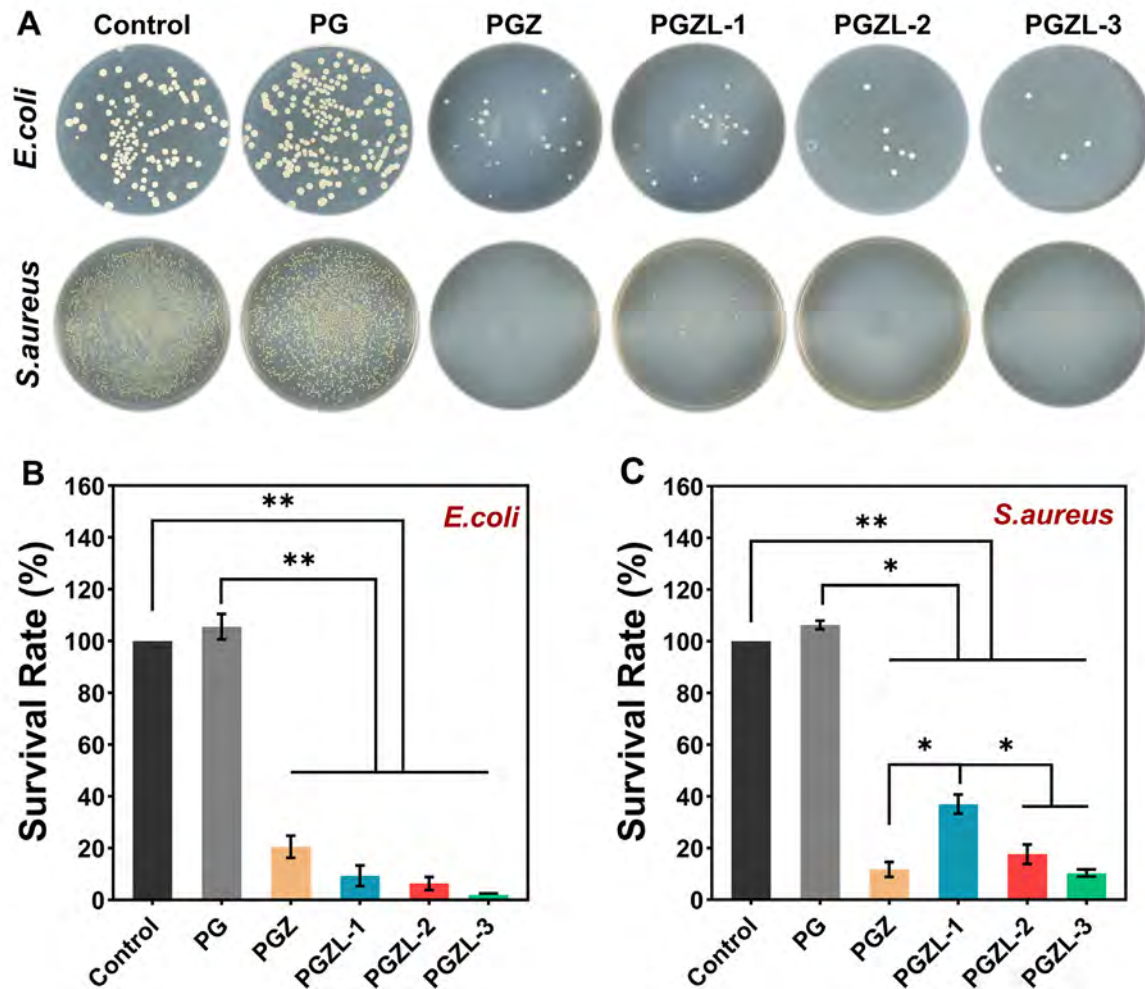
FIG. 7. Antibacterial properties of membranes ($n = 3$). (A) Visual diagram of colonies, (B) *E. coli* and (C) *S. aureus*. *$p < 0.05$ and **$p < 0.01$.

further revealed a significant improvement in the migration and tubule-like network formation of HUVECs, which are attributable to LG (Fig. 5). The LG can promote the phosphorylation of Akt, which may further regulate different cellular processes, including cell proliferation, chemotaxis, and vascularization by promoting the effects on epidermal growth factor (EGF) and transforming growth factor-beta (TGF-β) (8,10). Yu et al. (8) reported that the LG can promote the migration of keratinocytes by augmenting the phosphorylation of Akt and by activating PI3K/Akt pathway, which can induce wound regeneration *in vivo*. Similarly, LG can promote the VEGF expression of HUVECs as well as augment vascularization by activating miR-219b-3p mediated AKT/GSK-3β/β-catenin pathway (8). Consequently, LG may not only lead to more numbers of newly-formed blood vessels but may also increase the formation of mature blood vessels. Consequently, membranes containing ZnO-NPs and LG displayed good biocompatibility as well as promoted wound healing *in vitro*, which may also have implications for wound healing *in vivo*.

As most of the wounds bleed after injury, which may be life-threatening if not appropriately managed, hemostatic dressings may be helpful to overcome this issue (21). Zinc has been shown to mediate the coagulation pathway and affect hemostasis, plausibly by increasing the phosphorylation of protein kinase C in platelets, activating intrinsic and extrinsic coagulation pathways, and augmenting platelet activation and aggregation (18,19). We observed significantly less APTT values in membranes containing ZnO-NPs

and LG, which may fasten blood clotting for a better hemostatic ability (Fig. 6A, B and F). The higher hemostatic ability of membranes may also be attributed to the gelatin component of membranes, which can activate platelets aggregation and activation (22,23).

The exposure of the wound surface also increases bacterial infection risks on the wound surface, thereby perturbing and delaying the wound healing process. Previously, we and others have reported that varying concentrations of ZnO-NPs have a significant effect on the antibacterial activity (12,15). While the low concentrations of Zn may be insufficient to exert an antibacterial activity, the high concentrations of Zn may be toxic to the cells (15). Therefore, we used 1% of ZnO-NPs to fabricate membranes. Antibacterial test showed that the membranes containing both the ZnO-NPs and LG could efficiently inhibit the activity of the gram-positive bacteria *S. aureus* and gram-negative bacteria *E. coli* for up to 90% and 98%, respectively, which were significantly higher than that of the membranes devoid of ZnO-NPs and LG (Fig. 7). The improved antibacterial activity of membranes is attributable to the release of zinc ions (Zn^{2+}), which may not only interact with the negatively-charged bacterial membranes electrostatically but may also increase the permeability of bacterial cell membranes, thereby triggering bacterial cell death (24). Besides, ZnO-NPs can exert bactericidal effects via the decomposition of the bacterial outer membranes by reactive oxygen species and hydroxyl radicals (OH·), which may lead to phospholipid peroxidation and an ultimate apoptosis of bacterial species.
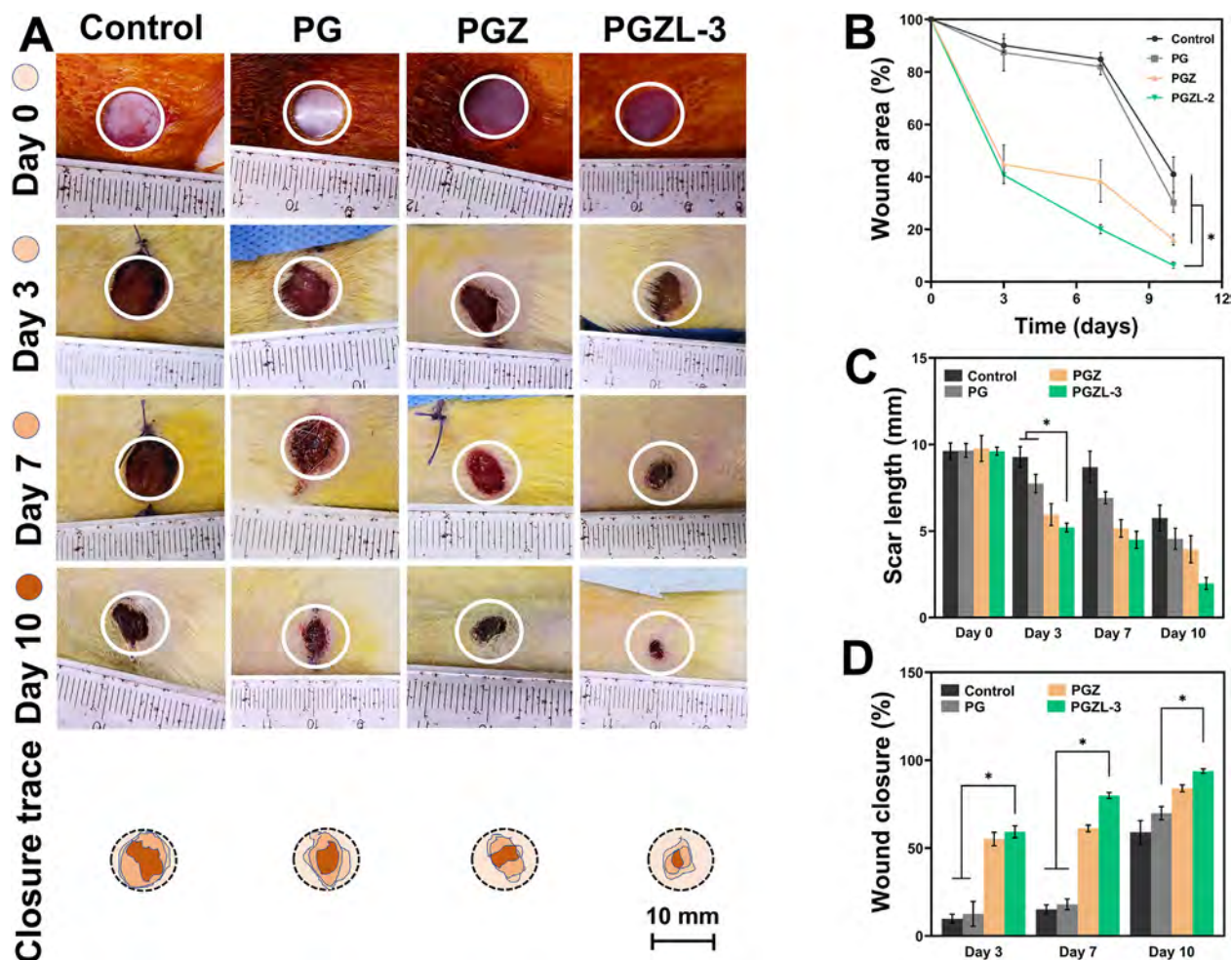
FIG. 8. Wound healing *in vivo*. Macroscopic images of *S. aureus*-infected full-thickness wounds treated with membranes (A), quantified wound area (B), scar length (C), and wound closure rate (D). *$p < 0.05$.

Besides, it has been previously reported that ZnO-NPs can physically adhere to bacterial cell wall to induce cell apoptosis (25).

To further exploit the potential of nanofibrous membranes for wound healing *in vivo*, we used *S. aureus*-infected rat wounds (Fig. 8). The wounds treated with the ZnO-NPs exhibited a higher wound-healing rate, which may be attributed to the significant inhibition of bacterial cell growth. By the day 10, under the combined influence of ZnO-NPs and LG, the percentage of wound area had reduced from 100% to only about 5%, and the length of the wound had also shrunk, showing a good degree of recovery (Fig. 8). The improved wound healing in an infection microenvironment could be ascribed to the synergistic effect of ZnO-NPs and LG, which may not only improve antibacterial and hemostatic processes but also affect the proliferation and migration of vascular cell types, thus leading to an accelerated wound healing (26–29). Yu et al. (8) reported LG-mediated increased wound healing, which was governed by an increased expression of PI3K/Akt pathway. Besides, the LG can increase the migration of keratinocytes in a dose-dependent manner and can promote the phosphorylation of Akt. Yu et al. (8) have also reported LG-mediated wound closure in a diabetic rat model.

Overall, these results showed that LG and ZnO-NPs acted synergistically to promote the proliferation and tubule-like network formation of HUVECs. Besides, ZnO-NPs/LG synergism improved the antibacterial and hemostatic properties of membranes *in vitro* as well as improved wound healing in a bacterial-infected wound model *in vivo*. There are also certain limitations in this study, such as the lack of a mechanistic insight, biocompatibility evaluation of membranes only by using HUVECs, and evaluation only in an infection model, which warrant further investigations.

References

1. **Chong, E. J., Phan, T. T., Lim, I. J., Zhang, Y. Z., Bay, B. H., Ramarkrishna, S., and Lim, C. T.:** Evaluation of electrospun PCL/gelatin nanofibrous scaffold for wound healing and dermal reconstitution, Acta Biomater., **3**, 321–330 (2007).

2. **Kamoun, E. A., Kenawy, S. R. S., and Chen, X.:** A review on polymeric hydrogel membranes for wound dressing applications: PVA-based hydrogel dressings, J. Adv. Res., **8**, 217–233 (2017).

3. **Li, M., Chen, J., Shi, M., Zhang, H., Ma, P. X., and Guo, B.:** Electroactive anti-oxidant polyurethane elastomers with shape memory property as non-adherent wound dressing to enhance wound healing, Chem. Eng. J., **375**, 121999 (2019).

4. **Yuan, Z., Sheng, D., Jiang, L., Khan, A., Shafiq, M., Hashim, R., Chen, Y., Li, B., Xie, X., Chen, J., and other 3 authors:** Vascular endothelial growth factor-capturing aligned electrospun polycaprolactone/gelatin nanofibers promote patellar ligament regeneration, Acta Biomater., **140**, 233–246 (2022).

5. **Yuan, Z., Ren, Y., Shafiq, M., Chen, Y., Tang, H., Li, B., El-Newehy, M., El-Hamshary, H., Morsi, Y., Zheng, H., and Mo, X.:** Converging 3D printing and electrospinning: effect of Poly(l-lactide)/gelatin based short nanofibers aero-gels on tracheal regeneration, Macromol. Biosci., **1**, e2100342 (2022).

6. **Ikegami, Y. and Ijima, H.:** Development of heparin-conjugated nanofibers and a novel biological signal by immobilized growth factors for peripheral nerve regeneration, J. Biosci. Bioeng., **129**, 354–362 (2020).

7. **Ikegami, Y., Mizumachi, H., Yoshida, K., and Ijima, H.:** Heparin-conjugated collagen as a potent growth factor-localizing and stabilizing scaffold for regenerative medicine, Regen. Ther., **15**, 236–242 (2020).

8. **Yu, M., Huang, J., Zhu, T., Lu, J., Liu, J., Li, X., Yan, X., and Liu, F.:** Liraglutide-loaded PLGA/gelatin electrospun nanofibrous mats promote angiogenesis to accelerate diabetic wound healing via the modulation of miR-29b-3p, Bio-mater. Sci., **8**, 4225–4238 (2020).

9. **Gaspari, T., Liu, H. B., Welungoda, I., Hu, Y., Widdop, R. E., Knudsen, L. B., Simpson, R. W., and Dear, A. E.:** A GLP-1 receptor agonist liraglutide inhibits endothelial cell dysfunction and vascular adhesion molecule expression in an ApoE$^{-/-}$ mouse model, Diabetes Vasc. Dis. Re., **8**, 117–124 (2011).

10. **Chen, Y., Zhang, X., He, J., Xie, Y., and Yang, Y.:** Delayed administration of the glucagon-like peptide 1 analog liraglutide promoting angiogenesis after focal cerebral ischemia in mice, J. Stroke Cerebrovasc. Dis., **27**, 1318–1325 (2018).

11. **Qi, W., Yang, C., Dai, Z., Che, D., Feng, J., Mao, Y., Cheng, R., Wang, Z., He, X., Zhou, T., and other 5 authors:** High levels of pigment epithelium-derived factor in diabetes impair wound healing through suppression of Wnt Signaling, Diabetes, **65**, 1407–1419 (2015).

12. **Shafiq, M., Yasin, T., Rafiq, M. A., and Shaista.:** : structural, thermal, and antibacterial properties of chitosan/ZnO composites, Polym. Compos., **35**, 79–85 (2014).

13. **Yu, L. P., Fang, T., Xiong, D. W., Zhu, W. T., and Sima, X. F.:** Comparative toxicity of nano-ZnO and bulk ZnO suspensions to zebrafish and the effects of sedimentation, $^{\cdot}$OH production and particle dissolution in distilled water, J. Environ. Monit., **13**, 1975–1982 (2011).

14. **Kumar, P. T. S., Lakshmanan, V.-K., Biswas, R., Nair, S. V., and Jayakumar, R.:** Synthesis and biological evaluation of chitin hydrogel/nano ZnO composite bandage as antibacterial wound dressing, J. Biomed. Nanotechnol., **8**, 891–900 (2012).

15. **Khan, A. R., Huang, K., Jinzhong, Z., Zhu, T., Morsi, Y., Aldalbahi, A., El-Newehy, M., Yan, X., and Mo, X.:** Exploration of the antibacterial and wound healing potential of a PLGA/silk fibroin based electrospun membrane loaded with zinc oxide nanoparticles, J. Mater. Chem. B, **9**, 1452–1465 (2021).

16. **Ghasemi-Mobarakeh, L. M. L., Prabhakaran, M. P., Morshed, M., Nasr-Esfahani, M. H., and Ramarkrishna, S.:** Electrospun poly(epsilon-caprolactone)/gelatin nanofibrous scaffolds for nerve tissue engineering, Bio-materials, **29**, 4532–4539 (2008).

17. **Augustine, R., Sarry, F., Kalarikkal, N., Thomas, S., Badie, L., and Rouxel, D.:** Surface acoustic wave device with reduced insertion loss by electrospinning P(VDF–TrFE)/ZnO nanocomposites, Nanomicro Lett., **8**, 282–290 (2016).

18. **Taylor, K. A. and Pugh, N.:** The contribution of zinc to platelet behaviour during haemostasis and thrombosis, Metallomics, **2**, 144–155 (2012).

19. **Marx, G., Krugliak, J., and Shaklai, M.:** Nutritional zinc increases platelet reactivity, Am. J. Hematol., **38**, 161–165 (2010).

20. **Cheng, J., Jun, Y., Qin, J., and Lee, S. H.:** Electrospinning versus microfluidic spinning of functional fibers for biomedical applications, Biomaterials, **114**, 121–143 (2017).

21. **Hsu, B. B., Conway, W., Tschabrunn, C. M., Mehta, M., Perez-Cuevas, M. B., Zhang, S., and Hammond, P. T.:** Clotting mimicry from robust hemostatic bandages based on self-assembling peptides, ACS Nano, **9**, 9394–9406 (2015).

22. **Xie, X., Li, D., Chen, Y., Shen, Y., Yu, F., Wang, W., Yuan, Z., Morsi, Y., Wu, J., and Mo, X.:** Conjugate electrospun 3d gelatin nanofiber sponge for rapid he-mostasis, Adv. Healthc. Mater., **10**, 2100918 (2021).

23. **Huang, Y., Zhao, X., Zhang, Z., Liang, Y., Yin, Z., Chen, B., Bai, L., Han, Y., and Guo, B.:** Degradable gelatin-based IPN cryogel hemostat for rapidly stopping deep noncompressible hemorrhage and simultaneously improving wound healing, Chem. Mater., **32**, 6595–6610 (2020).

24. **Du, Y., Zhang, J., Yan, S., Tao, Z., Wang, C., Huang, M., and Zhang, X.:** PEGylated zinc oxide nanoparticles induce apoptosis in pancreatic cancer cells through reactive oxygen species, IET Nanobiotechnol., **13**, 536–540 (2019).

25. **Rauf, M. A., Owais, M., Rajpoot, R., Ahmad, F., Khan, N., and Zubair, S.:** Biomimetically synthesized ZnO nanoparticles attain potent antibacterial ac-tivity against less susceptible *S. aureus* skin infection in experimental animals, RSC Adv., **7**, 36361–36373 (2017).

26. **Buysschaert, M., Baeck, M., Preumont, V., Marot, L., Hendrickx, M. E., Van Belle, A., and Dumoutier, L.:** Improvement of psoriasis during glucagon-like peptide-1 analogue therapy in type 2 diabetes is associated with decreasing dermal γδ T-cell number: a prospective case-series study, Br. J. Dermatol., **1**, 155–161 (2014).

27. **Cheng, L., Cai, Z., Ye, T., Yu, X., Chen, Z., Yan, Y., Qi, J., Wang, L., Liu, Z., Cui, W., and Deng, L.:** Injectable polypeptide-protein hydrogels for promoting infected wound healing, Adv. Funct. Mater., **30**, 2001196 (2020).

28. **Nasiry, D., Khalatbary, A. R., Abdollahifar, M. A., Bayat, M., Amini, A., Ashtiani, M. K., Rajabi, S., and Noori, A.:** SDF-1α loaded bioengineered human amniotic membrane-derived scaffold transplantation in combination with hyperbaric oxygen improved diabetic wound healing, J. Biosci. Bioeng., **133**, 489–501 (2022).

29. **Salles, G. N., Calio, M. L., Afewerki, S., Pacheco-Soares, C., Porcionatto, M., Holscher, C., and Lobo, A. O.:** Prolonged drug-releasing fibers attenuate Alz-heimer's disease-like pathogenesis, ACS Appl. Mater. Inter., **10**, 36693–36702 (2018).